

Solid-State Supramolecular Synthesis Based on the N–H...O Heterosynthon: An Approach to Solve the Polymorphism Problem in Famotidine

MARCOS G. RUSSO,¹ ELENA V. BRUSAU,¹ JAVIER ELLENA,² GRISELDA E. NARDA¹¹Química Inorgánica – INTEQUI. Facultad de Química, Bioquímica y Farmacia, Universidad Nacional de San Luis, San Luis 5700, Argentina²Physics Institute of São Carlos, University of São Paulo, São Carlos, São Paulo, CP 369, 13560-970, Brazil

Received 10 July 2014; revised 7 September 2014; accepted 12 September 2014

Published online in Wiley Online Library (wileyonlinelibrary.com). DOI 10.1002/jps.24196

ABSTRACT: Famotidine (FMT), a histamine H₂-receptor antagonist, is a drug commonly used in treatments of gastroesophageal diseases that presents solid-state polymorphism (A and B forms), the marketed form being the metastable polymorph B. A new stable salt was obtained by combination of FMT and maleic acid as cofomer. FMT maleate (FMT-MLT) was prepared either by solvent evaporation or comilling methods. Single-crystal X-ray diffraction reveals that (FMT)⁺ in FMT-MLT adopts an extended conformation that is stabilized by classical and nonclassical H-bonds. The three-dimensional packing consists of tapes along the axis *b* that further develop a columnar array based on H-bonds involving (FMT)⁺ side chain. Nonconventional π -stacking interactions between adjacent tapes were also identified. Fourier transform infrared, differential scanning calorimetry, thermogravimetric analysis, polarized light thermal microscopy, and scanning electron microscopy were employed to characterize the multicomponent complex. According to the solubility values in water and simulated gastric fluid, FMT-MLT exhibits such a performance that improves on the solubility of the commercially available polymorph. Finally, the higher stability of FMT-MLT regarding both FMT forms, as well as its easy preparation from either A or B forms or a mixture of them, also allows to consider this salt as a valuable alternative to avoid the polymorphism issue in marketed formulations containing FMT. © 2014 Wiley Periodicals, Inc. and the American Pharmacists Association *J Pharm Sci*

Keywords: crystal structure; solid state; thermal analysis; physicochemical properties; solubility; FTIR

INTRODUCTION

In recent years, the crystal engineering of pharmaceutical solids has achieved considerable development in the pharmaceutical industry.^{1–3} The design of new multicomponent solid-state assemblies, with improved properties, based on supramolecular synthons is the main goal in this area. The most common multicomponent systems of APIs (active pharmaceutical ingredients) are salts, which involves proton transfer from the acidic to the basic moiety, thus forming ionic components with opposite charges. On the contrary, cocrystals are obtained when proton transfer does not occur. The formation of a salt or a cocrystal depends upon the ΔpK_a of the API and the cofomer molecule. Several studies were carried out in order to evaluate the extent of proton transfer in the solid-state aiming to establish whether a salt, a cocrystal or a compound with mixed ionization states is obtained. Childs et al.⁴ propose a guideline known as “rule of three” that states that salts are expected if the ΔpK_a [$pK_{a(\text{base})} - pK_{a(\text{acid})}$] is greater than 2 or 3 units, whereas cocrystals will be obtained when ΔpK_a is negative. These ΔpK_a values were recently revised using crystallographic data from the Cambridge Structural Database and calculated pK_a s in Marvin for over 6000 acid base adducts.⁵ As a result, it is accepted that cocrystals or salts will be obtained if

$\Delta pK_a < -1$ or >4 , respectively, whereas in the ΔpK_a range -1 to 4 , salts, cocrystals, or compound containing mixed ionization states could be obtained.

It is well known that more than one-third of drug in pharmaceutical industry show polymorphism.^{6,7} Thus, even though the most stable solid form would be the recommendable one for solid dosage formulations to prevent phase transformations during the processing or storage, several cases of phase transitions have been reported when the therapeutically preferred but metastable form is used.^{8–11} Then, regulatory authorities encourage the pharmaceutical companies to investigate and control drug polymorphism to ensure product quality, safety, and performance.¹² Incorrect formulations containing mixtures of polymorphs also constitute another issue to solve. Such is the case of mebendazole, where not only the pharmacologically preferred form (C) but also the inactive one (A) were found in several marketed products.^{13,14} Two mebendazole salts with improved solubility were synthesized from either A, B, or C polymorphs.^{15,16} Thus, a simple reaction constitutes a valuable alternative to obtain a compound with appropriate properties able to avoid the polymorphism problem in pharmaceutical formulations. Famotidine (FMT), an orally active histamine H₂-receptor antagonist, is a classic example of conformational polymorphism.¹⁷ Two polymorphic forms have been previously reported, that is, the A form (A-FMT) that exhibits an extended conformation, and the B form (B-FMT) that adopts a folded one.¹⁸ The B polymorph is preferred for commercial formulations because of its physical properties that confer it higher bioavailability.¹⁹ However, it is a metastable form and therefore stability problems related to conversion to the more stable

Correspondence to: Griselda E. Narda (Telephone: +54-266-450300; E-mail: gnarda@unsl.edu.ar)

This article contains supplementary material available from the authors upon request or via the Internet at <http://onlinelibrary.wiley.com/>.

Journal of Pharmaceutical Sciences

© 2014 Wiley Periodicals, Inc. and the American Pharmacists Association

A form can be expected during processing and storage. It is noteworthy that polymorphic transformation from B- to A-FMT was achieved by the manual grinding method.²⁰ In addition, FMT belongs to class IV (low solubility and low permeability) according to the Biopharmaceutical System Classification²¹ and therefore its bioavailability is seriously limited. Several strategies have been developed to increase its solubility, such as preparation of solid dispersions,^{22,23} conversion to the amorphous state,²⁴ synthesis of inclusion complexes,^{25–27} and reduction of particle size.²⁸ However, the introduction of modifications at the molecular level of FMT by incorporating cofomers into a unique crystal lattice maintaining the covalent bonding of the API still remains an almost unexplored field. A strategy for the prediction and selection of drug substance salt forms was developed by Brittain.²⁹ Its utility was further demonstrated on FMT by predicting the existence of a number of salts and synthesizing one of them with salicylic acid as salt-forming agent. FMT salicylate exhibits much larger solubility than that of FMT and was characterized by powder X-ray diffraction (PXRD), IR spectroscopy, and differential scanning calorimetry (DSC) measurements.³⁰

In this work, crystal engineering concepts were taken into account to obtain a compound with improved properties in which the solid-state phase transition of the metastable B-FMT to the more stable A-FMT form could be avoided. To this end, maleic acid—a dicarboxylic acid that is pharmaceutically acceptable and appears on the GRAS (generally recognized as safe)³¹ list—was selected as cofomer as the carboxylic groups are potential candidates to participate in supramolecular heterosynthons with FMT. Thus, single crystals of FMT maleate (FMT-MLT) were obtained from recrystallization of FMT in a maleic acid methanolic solution. Additionally, FMT-MLT microcrystalline powder was also obtained by the comilling process, broadly accepted in the pharmaceutical industry. The milling time was standardized by the relative degree of crystallinity (RDC%) analysis. FMT-MLT was fully characterized and the results were compared with those corresponding to A and B polymorphic forms of FMT. To this aim, solid-state techniques such as Fourier transform infrared (FTIR), PXRD, DSC, thermogravimetric analysis (TGA), Polarized light thermal microscopy, and scanning electron microscopy (SEM) were employed. Finally, the solubility values in water and simulated gastric fluid (SGF) were determined employing the shake-flask procedure.

EXPERIMENTAL

Material

Famotidine (MW: 337.4 g/mol) was purchased as a polymorphic mixture of A and B forms from Fluka Analytical® (Sigma-Aldrich Co, St. Louis, Missouri) and used as received for all synthesis processes. The pure A and B polymorphs were obtained as described in Hassan et al.³² and tested by comparing the corresponding powder X-ray diagrams and IR spectra with those reported in the literature.¹⁹

Synthesis of FMT-MLT

Solvent Evaporation Method

A solution containing 109 mg (0.3 mmol) of FMT (A–B forms mixture) in 50 mL of boiling anhydrous methanol was added to the same volume of a methanolic maleic acid solution

(40.22 mg, 0.3 mmol) and vigorously stirred for 60 min. The resulting solution was kept for 2 days at 25°C yielding colorless needle-shaped crystals, suitable for the crystallographic characterization. The synthesis from the pure A or B forms led to identical results. In addition, FMT-MLT was also obtained as polycrystalline powder from other solvents as boiling water and absolute ethanol. The obtained products were filtered, washed with hexane–methanol (10:1), and dried under room conditions for further characterization.

Comilling Method

Famotidine (436 mg, 1.2 mmol) and maleic acid (278.4 mg, 1.2 mmol) were comilled using an oscillatory ball mill Mixer Mill MM400 RETSCH (Retsch GmbH, Haan, Germany). The sample powder was placed in a 25-mL volume stainless steel milling jar containing two 7-mm diameter stainless steel balls and milled at a frequency of 25 Hz. Milling was conducted in a room at $25 \pm 2^\circ\text{C}$ for 180 min; the jar was immersed into liquid nitrogen each 40 min. The crystallinity of the samples at different milling times was evaluated by PXRD using the RDC analysis. RDC could be defined as the $I_{\text{SA}}/I_{\text{REF}}$ ratio, where I_{SA} is the diffraction peak height of the sample under study, whereas I_{REF} is the peak height at the same angle (2θ) of a reference. The intensity of the peak at 20.54 2θ angle in the experimental diffractogram of FMT-MLT obtained by the solvent evaporation method was taken as I_{REF} in the present case.

Methods

Single-crystal X-ray diffraction measurements were carried out at 100(2) K on a Bruker APEX II-DUO Diffractometer (Bruker Corporation, MA) equipped with Bruker Kryoflex open flow cryostat enabling low-temperature data collection using $\text{CuK}\alpha$ radiation (1.5418 Å). Unit cell determination, data collection, and integration were obtained with APEX II and SAINT software (Bruker Corporation, MA).^{33,34} Multiscan absorption corrections were applied using SADABS program based on Blessing's method.^{35,36} The structure was solved by direct methods with SHELXS-97 and all nonhydrogen atoms were anisotropically refined by full-matrix least-squares techniques on F^2 using SHELXL-97.^{37,38} The C–H hydrogen atoms were stereochemically positioned and refined with fixed individual displacement parameters [$U_{\text{iso}}(\text{H}) = 1.2 U_{\text{eq}}(\text{Csp}^2)$ or $1.5 U_{\text{eq}}(\text{Csp}^3)$] using a riding model with aromatic C–H bond length of 0.93 Å and methylene C–H one of 0.97 Å. The N–H, N⁺–H, and O–H hydrogen atoms were found in the difference Fourier map and their positions freely refined with fixed isotropic thermal parameters [$U_{\text{iso}}(\text{H}) = 1.2 U_{\text{eq}}(\text{N})$ or $1.5 U_{\text{eq}}(\text{O})$].

Positional disorder in C(10) and C(11) atoms was satisfactorily solved. Different populations of disordered conformers labeled as A (60%) and B (40%) occur in two opposite orientations across the screw axis. Considering that the crystal is a twin, the twin orientation matrix and the refined twin ratio (defined as the fractional contribution of each twin component) that allow the structural solution were found to be (1 0 1 0 -1 0 0 0 -1) and 0.4, respectively. Crystalline habit of the FMT-MLT exhibiting its twin nature is shown in Figure S1. The analysis of the intramolecular geometric parameters of (FMT)⁺ in FMT-MLT was performed with MOGUL³⁹ applying the following filters: *R* factor less than 5% and exclusion of metal–organic compounds. SHELXL-97,^{37,38} ORTEP-3,⁴⁰ and MERCURY⁴¹

programs were used within WinGX⁴² to prepare materials for publication. The crystallographic information file (CIF) loading the data sets (excluding the structure factors) for FMT-MLT has been deposited in the Cambridge Structural Data Base under deposit code CCDC 1012192 (copies of these data may be obtained free of charge from The Director, CCDC, 12 Union Road, Cambridge CB2 1EZ, UK, fax: 44–123–336–033; e-mail: deposit@ccdc.cam.ac.uk or <http://www.ccdc.cam.ac.uk>).

Fourier transform infrared spectra were recorded on a Nicolet PROTÉGÉ 460 Spectrometer (Nicolet Instrument Corporation, Madison, Wisconsin) provided with a CsI beamsplitter in the 4000–400 cm^{-1} range with 64 scans and spectral resolution of 2 cm^{-1} using the KBr pellet technique.

X-ray powder diffraction diagrams were obtained with a Rigaku ULTIMA IV diffractometer (Rigaku Co, Tokyo, Japan) using $\text{CuK}\alpha$ radiation (Ni-filter) and NaCl and quartz as external calibration standards. The diffractograms were recorded in the 2θ angle range 3° – 45° and the process parameters were set at 0.02 2θ scan step size and 2 s scan step time.

Differential scanning calorimetry curves were obtained with a Shimadzu TA-60WS Thermal Analysis System (Shimadzu Inc., Kyoto, Japan) using 3–5 mg of each sample in open aluminum pans with flowing air at 50 mL/min and a heating rate of $10^\circ\text{C}/\text{min}$ from room temperature (RT) to 200°C . Calibration of the DSC instrument was carried out using indium as standard. The T_g (glass transition temperature) was determined as the midpoint of the change in heat capacity of the samples, whereas both T_c (crystallization temperature) and T_m (melting temperature) were determined as the onset temperatures. The DSC analysis allows the monitoring of the solid-state modifications as a function of the milling time of the comilled samples. Each assay was performed in triplicate.

Thermogravimetric analysis was performed using a Shimadzu TGA-51 Thermal Analyzer (Shimadzu Inc., Kyoto, Japan) using platinum pans, flowing air at 50 mL/min and a heating rate of $10^\circ\text{C}/\text{min}$ from RT to 800°C .

Polarized light thermal microscopy experiments were performed in a Linkam Hot-Stage system, model THMS600 equipped with a Leica DM2500 microscope and a Pixelink PL-A662 video camera (Linkam Scientific Instruments Ltd, Merstham, United Kingdom). LINKSYS 32 DV-NC system software by Linkam was used for temperature control and image record and analysis. Images were obtained by the combined use of polarized light and wave compensators using a $10\times$ magnification.

Scanning electron microscopy technique was used to observe and analyze the morphology of the samples that were mounted on double-sided carbon adhesive tapes on aluminum stubs and gold coated (30 nm thickness) and processed in a standard sputter prior to observation in a LEO1450VP (LEO Electron Microscopy Ltd., Clifton Road, England).

Solubility Assays

Equilibrium solubility studies were performed for FMT-MLT and compared with A and B forms of FMT. Assays were carried out in distilled water and SGF free of enzymes. The SGF medium consists of a HCl/KCl (0.05 mol/L) acid buffer solution at pH 2. An excess of the drugs was added into Eppendorf® tubes with 1.5 mL of dissolution medium. These aqueous suspensions were shaken in a JEIO TECH SI-300R Shaker (JEIO

TECH Co. Ltd. Seoul, Korea) at 100 rpm at 37°C during 24 and 1 h for water and SGF, respectively (see section *Solubility Assays* in Results). The resulting suspensions were filtered with a 0.22- μm Millipore® (MERCK KGaA, Darmstadt, Germany) membrane filters. The FMT concentration in the filtrate was determined at 276 nm using a Shimadzu UV-160 A spectrophotometer (Shimadzu Inc., Kyoto, Japan) with CPS-240A cell positioned using quartz cells (light-path = 10 mm); the temperature was maintained at $25.0 \pm 1^\circ\text{C}$ during the measurements. Appropriate dilutions had to be prepared to fit the linear range of 0.0105–0.0642 mg/mL. The solubility of each sample was determined by triplicate. The calibration curve is shown in Figure S2.

RESULTS

Crystal Structure Description

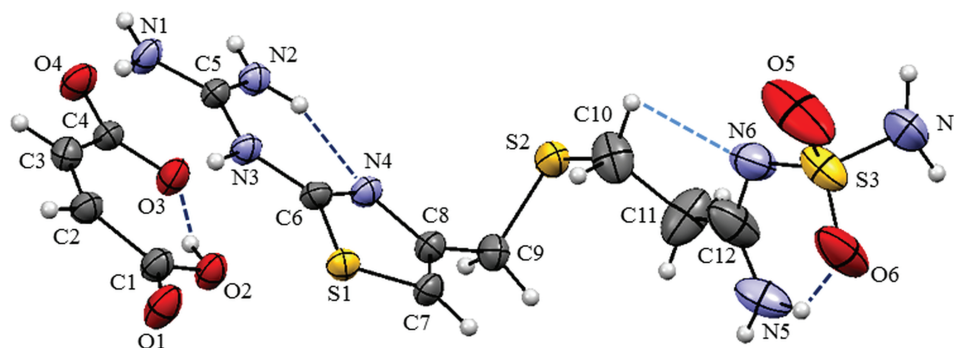
The experimental PXRD diagram fits well with the theoretical one obtained by simulation with MERCURY⁴¹ inputting the FMT-MLT CIF created after the structure refinement (Fig. S3). Table 1 lists the data collection and refinement details from the single-crystal X-ray diffraction experiment. Figure 1 shows an ORTEP-3⁴⁰ view of the asymmetric unit of FMT-MLT that contains one (FMT)⁺ and one (MLT)[−] ions. The intramolecular hydrogen bonds in the asymmetric unit with their respective distances and angles are listed in Table 2.

The intra- and intermolecular H-bonds involving the sulfamoyl group ($-\text{SO}_2\text{N}_2$) in FMT-MLT are responsible for the distorted tetrahedral geometry observed around the sulfur atom. The geometrical parameters of $-\text{SO}_2\text{N}_2$ are listed in Table S1. The structural analysis of the methylthiopropyl side chain of (FMT)⁺ in FMT-MLT shows an extended conformation, similar to that found in A-FMT. The dihedral angles of (FMT)⁺ in FMT-MLT and A-FMT are summarized in Table 3. As can be seen, the dihedral angles are comparable in both compounds except for ω_4 that is significantly higher for the salt revealing that the methylthiopropyl chain of (FMT)⁺ adopts a more extended conformation (see Fig. S4).

The guanidine moiety in FMT contains three nitrogen atoms susceptible of being protonated. The $n-\pi$ possible conjugations between the amino and imino N atoms increase the basicity of the N-imine atom and decrease the basicity of the N-amine ones.⁴³ This is in agreement with the protonation of the N(3) atom observed in the FMT-MLT difference Fourier map, as expected from the corresponding ΔpK_a (5.14) and the calculated high degree of efficiency for salt formation,³⁰ resulting in the highly stable guanidinium group. The higher stability of this group arises from both the Y-aromaticity and the favorable positive charge distribution.⁴³ The CN bond lengths and the angular values are not equal as it would be expected for a free guanidinium group; in fact, they are significantly different as a consequence of not only the substitution (i.e., thiazole ring), but also the presence of intra- and intermolecular H-bonds. An intramolecular H-bond is observed between N(2) and N(4) atoms (see Table 2), thus forming a six-membered ring. This interaction is stabilized by the resonance-assisted hydrogen bond (RAHB) effect involving the H(2A)–N(2)–C(5)–N(3)–C(6)–N(4) atoms.^{44,45} Moreover, it is the responsible of the coplanarity observed between the thiazole ring and the guanidinium group (see Fig. S5).

Table 1. Crystal Data and Structure Refinement for FMT-MLT

Empirical Formula	$C_{12}H_{19}N_7O_6S_3$	
Temperature	100.0(2) K	
Formula weight	453.55	
Wavelength (Å)	1.54178	
Crystal system	Monoclinic	
Space group	$P2_1/c$	
Unit cell dimensions (Å, °)	$a = 17.6489(13)$ $b = 15.3720(10)$ $c = 7.0841(7)$	$\beta = 101.581(7)$
Volume (Å ³)	1882.8(3)	
Z	4	
Density (calculated) (mg m ⁻³)	1.600	
Absorption coefficient (mm ⁻¹)	4.044	
F(000)	944	
Crystal size (mm)	0.24 × 0.04 × 0.04	
θ range	5.76–67.2	
Index ranges	$-21 \leq h \leq 20$, $-17 \leq k \leq 18$, $-8 \leq l \leq 7$	
Collected reflections	11,273	
Independent reflections	3163 [Rint = 0.0881]	
Completeness to $\theta = 67.20$	94.0%	
Refinement method	Full-matrix least-square on F^2	
Absorption correction	1.000–0.749	
Data/restraints/parameters	3163/0/272	
Goodness-of-fit on F^2	1.058	
Final R indices [$I > 2\sigma(I)$]	R1 = 0.0595, wR2 = 0.1550	
R indices (all data)	R1 = 0.0722, wR2 = 0.1721	
Largest difference peak and hole (e. Å ⁻³)	0.58 and -0.65	

**Figure 1.** ORTEP-3 view of the asymmetric unit of FMT-MLT showing the atoms labeling, the 50% probability ellipsoids, and classical (blue dashed lines) and nonclassical (blue light dashed lines) H-bond interactions.

The maleic acid moiety adopts a nearly planar conformation according to the dihedral angle C(1)–C(2)–C(3)–C(4) of $-2.90(1)^\circ$. In addition, an intramolecular H-bond involving the O(3) atom and the C(1)–O(1)–O(2)–H carboxylic group, forming a seven-membered ring, is observed (Table 2).

The crystal structure presents a three-dimensional packing stabilized by a complex pattern of H-bond intermolecular interactions as can be seen from Figure 2. The corresponding geometrical parameters are listed in Table 2. Each (FMT)⁺ in the FMT-MLT interacts with two cofomer molecules through N(1)–H(1B)⋯(O4), N(1)–H(1A)⋯O(2), N(2)–H(1A)⋯O(1), and N(3)–H(3N)⋯(O3) H-bonds, giving rise to the formation of two heterosynthons N–H⋯O (Fig. 2a) exhibiting a $R_2^2/8$ motif. These interactions are responsible for the deviation in the N(1)–C(5)–N(2) bond angle when compared with the expected values from the statistical analysis performed using MOGUL³⁹

program (Fig. S6). The H-bonds previously described involving all the N atoms of the guanidinium group lead to the formation of infinite tapes along the b axis (Fig. 2b). Each methylthiopropyl side chain of (FMT)⁺ in FMT-MLT interacts through H-bonds (see Fig. S7), thus leading to the three-dimensional packing. The N(5)–H(5B)⋯O(5) H-bond connects the primary amine of the side chain of (FMT)⁺ with the O(5) atom of the sulfamoyl group of another (FMT)⁺ determining columns along the c axis that are further linked by the N(5)–H(5A)⋯O(6) intermolecular H-bond. Finally, π – π stacking interactions between adjacent tapes are observed in the three-dimensional packing. However, it is interesting to note that in FMT-MLT, these interactions are not the conventional ones, that is, between two ordinary aromatic rings. They can be described as hybrid π – π stacking interactions because they occur between a quasaromatic ring (formed as a result of the RAHB effect) and

Table 2. Geometrical Parameters of the Intra- and Intermolecular Hydrogen Bonds (with e.s.d.'s in Parenthesis) of FMT-MLT

D–H...A	D–H (Å)	D...A (Å)	H...A (Å)	D–H...A (°)
Intramolecular H-bonds				
N(2)–H(2B)...N(4) ^a	0.860	2.725(6)	2.066	132.9
N(5)–H(5A)...O(6) ^a	0.860	2.707(10)	2.063	131.1
O(2)–H(2M)...O(3) ^a	1.100	2.420(5)	1.392	152.1
C(10)–H(10A)...N6 ^a	0.970	2.980(17)	2.795	91.3
Intermolecular H-bonds				
N(1)–H(1B)...O(4) ^a	0.860	2.881(6)	2.027	171.7
N(3)–H(3N)...O(3) ^a	0.896	2.749(5)	1.868	167.2
N(2)–H(2A)...O(1) ^b	0.860	2.817(5)	1.963	171.6
N(1)–H(1A)...O(2) ^b	0.860	2.927(5)	2.082	167.0
N(5)–H(5A)...O(6) ^c	0.860	2.958(9)	2.527	112.0
N(5)–H(5B)...O(5) ^d	0.860	2.959(10)	2.122	164.3

Symmetry operations: a) x, y, z ; b) $x, -y+1/2, +z+1/2$; c) $-x+1, -y+1, +z+1$; d) $x, -y-1/2, z+1/2$.

D, donor; A, acceptor.

an ordinary aromatic ring.⁴⁶ In our case, the hybrid π - π stacking interaction is observed between the previously described H(2A)–N(2)–C(5)–N(3)–C(6)–N(4) ring and the thiazole ring (see Fig. 2b). The distances between centroids (Ct) are 3.497 Å for Ct1–Ct2 and 3.623 Å for Ct1'–Ct2' that indicates that adjacent chains are not completely parallel. The displacement angles are 3.91° and 3.38° for Ct1–Ct2 and Ct1'–Ct2', respectively, determining a nearly cofacial orientation between both rings.

Table 3. Dihedral Angles of the Methylthiopropyl Side Chain in A-FMT and FMT-MLT (with e.s.d.'s in Parenthesis)

Angle Denomination	Fragment	A-Form (°) ^a	FMT-MLT (°)
$\Omega 1$	N(4)–C(8)–C(9)–S(2)	–79.17(3)	–65.00(6)
$\Omega 2$	C(8)–C(9)–S(2)–C(10)	–71.51(3)	–68.10(6)
$\Omega 3$	C(9)–S(2)–C(10)–C(11)	–83.34(2)	–79.39(1)
$\Omega 4$	S(2)–C(10)–C(11)–C(12)	68.03(3)	175.84(9)

^aFrom Overgaard et al.¹⁸

FTIR Analysis

The FTIR spectra of FMT-MLT, A-FMT, and B-FMT are displayed in Figure 3. Because of their complexity, the analysis is focused in those FMT functional groups directly involved in the intermolecular interactions with the maleic acid (see Table S2). Expected differences were found in the FMT-MLT spectrum when it was compared with those of FMT polymorphs. The broad band centered at 3425 cm^{-1} that is associated with the (NH) mode of the guanidinium group is shifted to lower frequencies in FMT-MLT spectrum while the corresponding $\delta(\text{NH})$ mode appears at higher ones. These shifts are consistent with the presence of several H-bonds in the crystal lattice mainly involving the guanidinium group of (FMT)⁺ and the (MLT)[−]. Moreover, we propose that the broad feature of the former band is because of the contribution of the $\nu(\text{O}-\text{H})$ belonging to the carboxylic group; the lowering in its frequency value when compared with that of the free carboxylic group

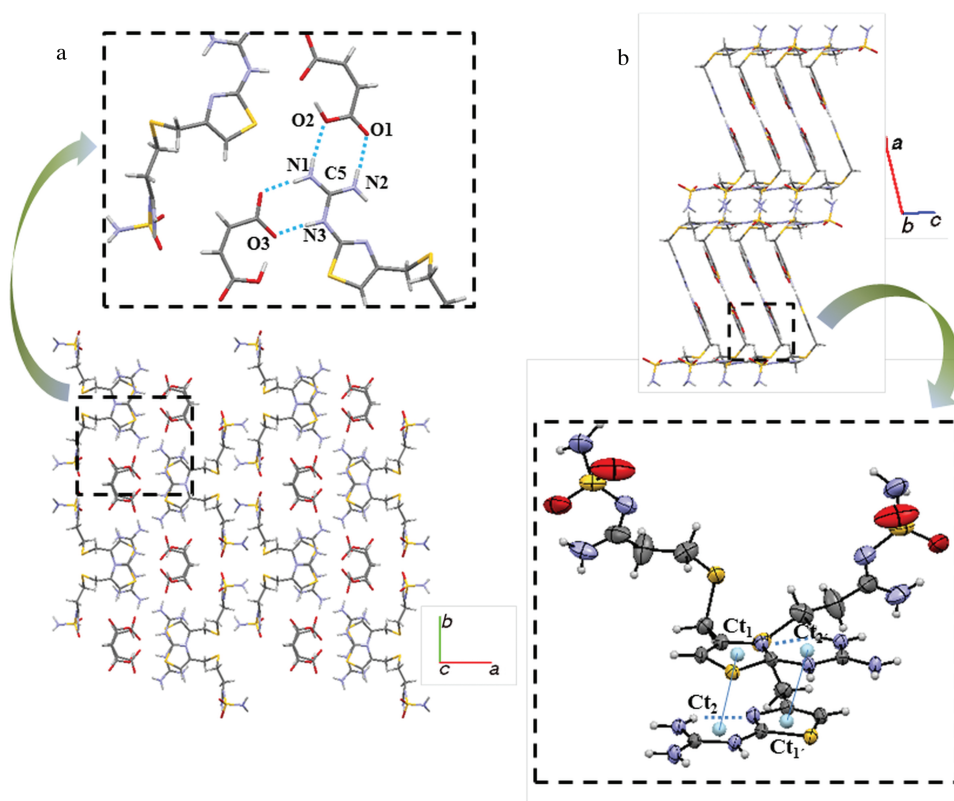


Figure 2. Famotidine-MLT crystal packing. (a) View along the c axis (the intermolecular H-bond interactions in guanidinium group are displayed in light blue). (b) View along the b axis.

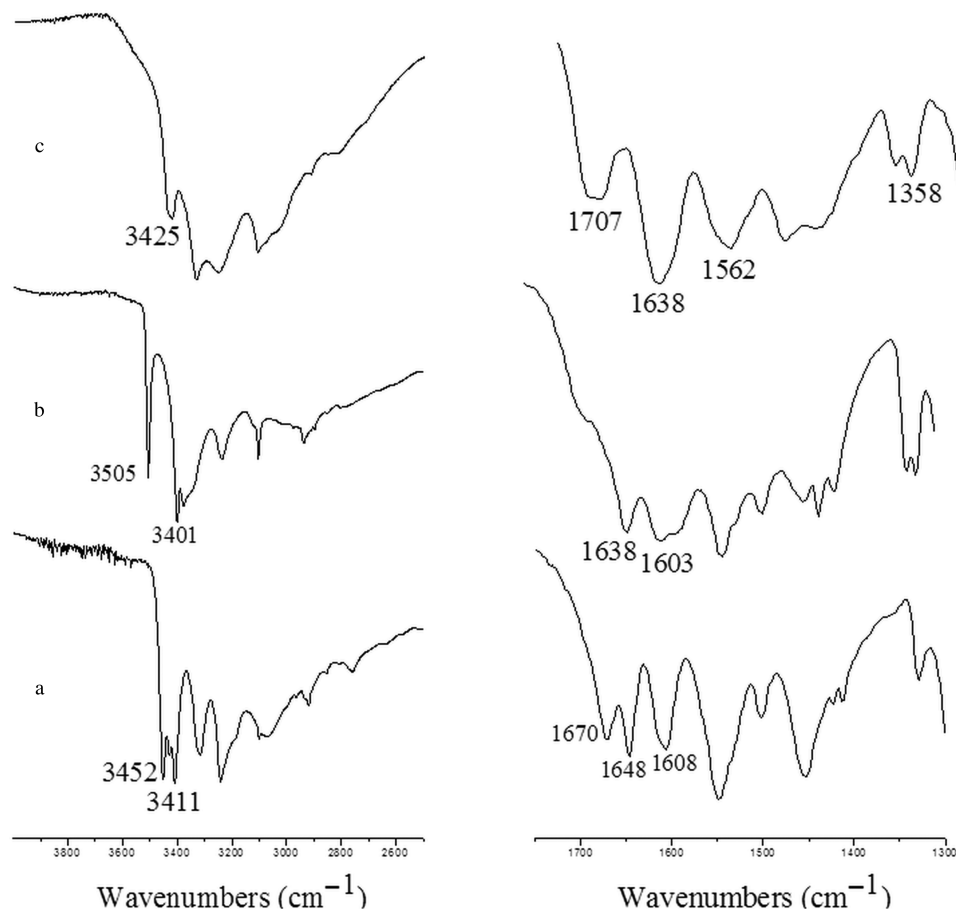


Figure 3. Fourier transform infrared spectra of (a) A-FMT, (b) B-FMT, and (c) FMT-MLT.

(assigned in the range 3560–3500 cm^{-1}) is associated with the (O(2)–H(2M)⋯O(3)) intramolecular H-bond between the carboxylate and carboxylic groups of the MLT ion (see Fig. 1). Regarding the $\nu(\text{C}=\text{N})$ mode, it appears in the region comprised between 1640 and 1560 cm^{-1} . A band at 1562 cm^{-1} in the FMT-MLT spectrum is assigned to the $\nu\text{N}(1)\text{--C}(5)$ and $\nu\text{N}(2)\text{--C}(5)$ modes, whereas the $\nu\text{N}(3)\text{--C}(5)$ one occurs at 1638 cm^{-1} . The assignment is in agreement with the structural data that determines similar bond distances for N(1)–C(5) and N(2)–C(5) and a shorter one for the N(3)–C(5) bond in the guanidinium group.

The bands originated in the vibrational modes of the carboxylic and carboxylate groups can also be identified in the FMT-MLT spectrum. The band centered at 1707 cm^{-1} is assigned to $\nu[\text{C}(1)=\text{O}(1)]$ mode of the former group. The $\nu_{\text{as}}[\text{O}(4)\text{--C}(4)\text{--O}(3)]$ mode is associated with a broad band centered at 1562 cm^{-1} —overlapped with the $\nu(\text{C}=\text{N})$ mode—whereas the corresponding symmetric mode is assigned to the band located at 1358 cm^{-1} .

Thermal Analysis

Figure 4a displays the DSC profile of FMT-MLT in comparison with the corresponding ones of A- and B-FMT. The melting processes of both polymorphs are consistent with those reported in the literature,^{25,32,47,48} the melting points being $171.04 \pm 0.98^\circ\text{C}$ and $161.55 \pm 1.23^\circ\text{C}$ for A-FMT and B-FMT, respectively. A higher thermal stability is evidenced for FMT-MLT as

the melting process occurs at $186.09 \pm 0.86^\circ\text{C}$, approximately 15°C higher than the more stable polymorph. Additionally, the hot-stage microphotographs are in good agreement with the DSC data (Fig. 4b).

Thermogravimetric analysis indicates that FMT-MLT decomposes in two well-defined steps (Fig. S8), the first one corresponding to a 35.13% weight loss (calculated: 33.29%; on set: 191.53°C). In an attempt to elucidate this process, a small amount of sample was heated at the appropriate temperature and then the corresponding FTIR spectrum was recorded. The absence of the IR bands derived from the SO_2 modes, the presence of the $\nu[\text{C}(1)=\text{O}(1)]$, belonging to the cofomer, as well as the band at 1502 cm^{-1} , corresponding to $\nu(\text{thiazole})$,⁴⁹ confirm the breakdown of the S(2)–C(10) bond (see Scheme S1). In the second step, a mass decay of 63.65% (calculated: 64.84%; on set: 516.89°C) is observed, leading to the complete decomposition of the compound.

Synthesis of FMT-MLT by the Comilling Process

The solid-state preparation of new molecular complexes with improved properties by interaction of an API and a suitable cofomer offers several advantages such as a more environmentally friendly synthesis, an experimental design free from solubility considerations,⁵⁰ and most importantly it has become the preferred methodology for industrial-scale processes in the pharmaceutical industry. Thus, the comilling method was also probed for the system FMT–maleic acid, and FMT-MLT was

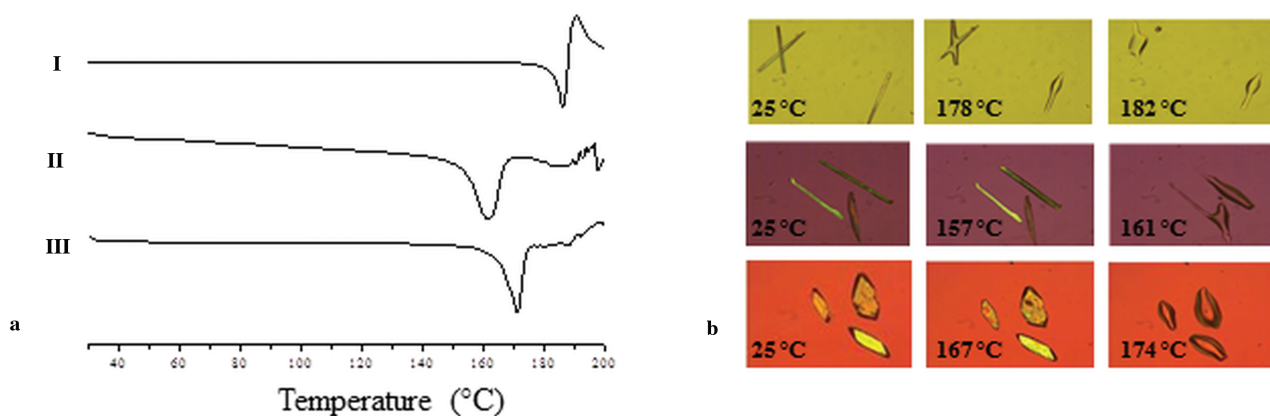


Figure 4. (a) Differential scanning calorimetry profiles and (b) hot-stage microphotographs of (I) A-FMT, (II) B-FMT, and (III) FMT-MLT.

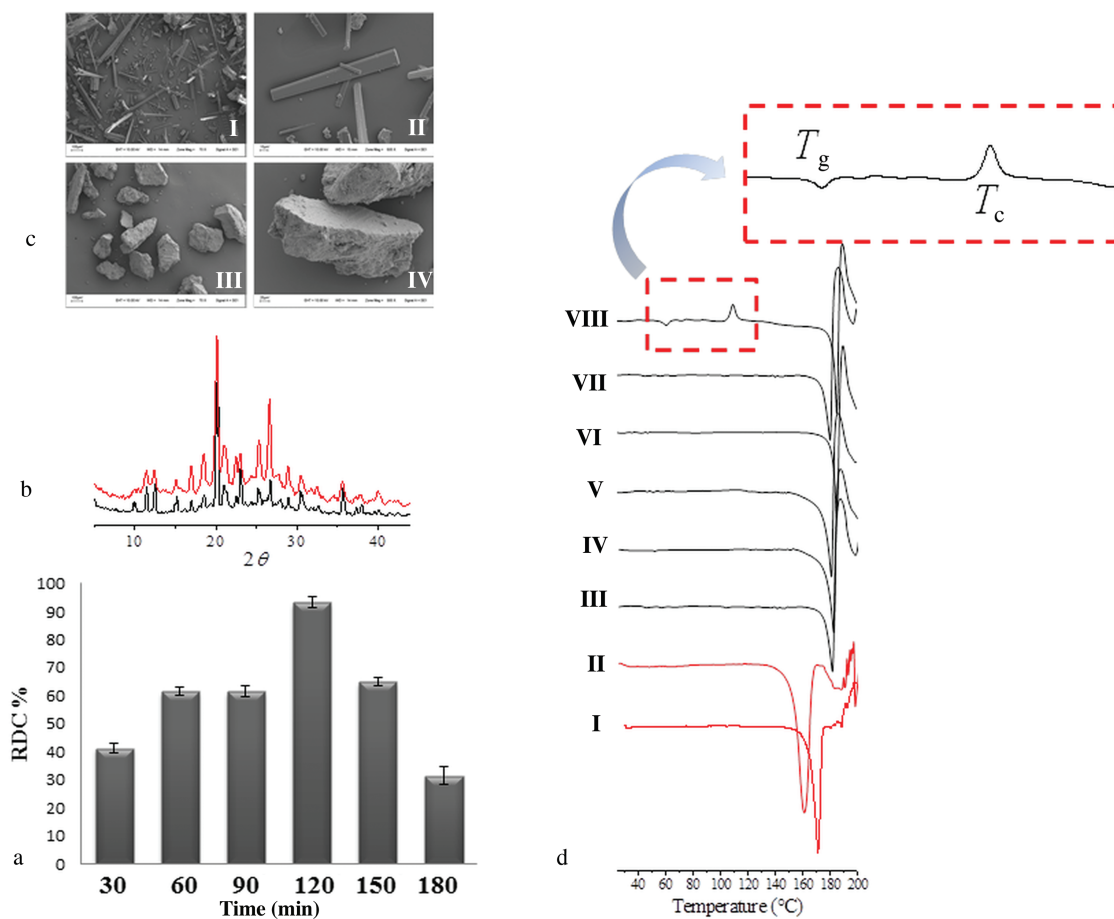


Figure 5. (a) Bar diagram of RDC ($n = 3$). (b) PXRD of FMT-MLT obtained by solvent evaporation method versus FMT-MLT obtained at 120 min of milling. (c) SEM microphotographs of FMT-MLT and FMT-MLT_{CM}. (I) and (II) FMT-MLT at 70 \times and 500 \times , respectively. (III) and (IV) FMT-MLT_{CM} at 70 \times and 300 \times , respectively. (d) DSC profiles at different milling times. (I) A-FMT, (II) B-FMT, (III) 30 min, (IV) 60 min, (V) 90 min, (VI) 120 min, (VII) 150 min, and (VIII) 180 min of milling.

Table 4. Solubility Values in Water and SGF (mg mL^{-1})

Medium Dissolution	FMT A	FMT B	FMT- MLT	FMT- MLT _{CM}
Water	0.768 ± 0.007	0.984 ± 0.068	1.239 ± 0.049	1.241 ± 0.029
SGF	1.280 ± 0.072	1.667 ± 0.059	2.798 ± 0.330	2.510 ± 0.293

obtained according to the PXRD patterns at different times of the milling process shown in Figure S9; the diffractograms of A-FMT and B-FMT are also included for comparison. As can be seen, the powder diagrams recorded every 30 min of milling do not show the diffraction peaks corresponding to the initial reagents and only the diffraction peaks characteristic of FMT-MLT are observed. These diffraction peaks remain up to 150 min of milling, whereas a poorly crystalline sample is obtained at 180 min. As the milling time modifies the crystallinity, the RDC% was calculated to optimize the time where the most crystalline FMT-MLT is obtained. Taking into account the results of the RDC% values at different milling times displayed in Figure 5a, the crystallinity of the sample at 120 min is similar to that corresponding to the compound obtained by the solvent evaporation method (Fig. 5b). So, further analyses described here were performed on this sample, named FMT-MLT_{CM} from now on. In order to determine whether crystallinity of FMT-MLT_{CM} remains over time and also at different temperatures, the polycrystalline powder was placed under dry conditions in a desiccator at 4°C, 25°C, and 40°C for 60 days. It was verified that the crystallinity is retained during that period at all tested temperatures (Fig. S10). This high stability is attributed to a solid-state reaction (acid-base reaction) between both reagents during the milling process.⁵¹

The SEM microphotographs of FMT-MLT in comparison with those of FMT-MLT_{CM} are shown in Figure 5c. The cogrinding process produces a larger particle size than that obtained by the solvent evaporation method. Besides, FMT-MLT crystallizes as planar bars, whereas FMT-MLT_{CM} exhibits a nonregular block shape that is more appropriate for develop formulations. Additionally, the vibrational and thermal behaviors of FMT-MLT_{CM} and FMT-MLT are identical. Figure S11 shows the FTIR spectra and DSC curves of both compounds.

To investigate the eventual formation of an amorphous compound during the comilling process, DSC analysis was performed in order to find thermal properties inherent to poorly crystalline compounds (i.e., T_g and T_c). The DSC diagrams up to 200°C at different milling times are displayed in Figure 5d. The DSC curves of A- and B-FMT were also included for comparison. According to the DSC analysis, the thermal behavior of the comilled samples at different intervals studied is consistent with that observed for FMT-MLT (see section *Thermal Analysis*). Moreover, no traces of the reagents were detected, that is, melting, this fact being indicative of complete reaction between FMT and maleic acid. Additional signals to those corresponding to the melting and decomposition processes are only observed in the sample obtained at 180 min of milling (Fig. 5d, VIII). First, a weak endothermic signal at $59.35 \pm 1.32^\circ\text{C}$ is attributable to the T_g , whereas the exothermic event at $113.38 \pm 0.87^\circ\text{C}$ could be associated to T_c . These data are in agreement with the PXRD results that demonstrate the lowest crystallinity for the sample milled during 180 min.

Solubility Assays

The solubility values determined in water for FMT-MLT and FMT-MLT_{CM} along with those for both FMT polymorphs are gathered in Table 4. The water solubility values of A-FMT and B-FMT are in agreement with those previously reported.⁵² FMT-MLT presents higher solubility than the polymorphs of the parental drug as increments of 1.68 and 1.25 times are ob-

served when compared with the A- and B-FMT, respectively. No significant differences in the solubility values were found between FMT-MLT and FMT-MLT_{CM}.

As FMT is absorbed in the stomach cavity, the solubility assays in water do not represent the gastrointestinal conditions. To clarify that, the solubility was also measured in SGF. However, under these conditions (pH 2, 37°C), FMT is highly unstable. Taking into account the degradation kinetics proposed by Wu and Fassihi,⁵³ we determine the solubility at 60 min because of the degradation products are kept to minimum (less than 5%) in that period. The corresponding data are collected in Table 4. An increase in the solubility values in SGF versus water is evident in all cases. FMT-MLT shows increments of 1.67 and 1.23 times compared with A- and B-FMT, respectively, whereas FMT-MLT_{CM} exhibits a similar performance.

CONCLUSIONS

Crystalline engineering concepts were employed to overcome the polymorphism issue of FMT by obtaining a new FMT salt with improved solubility and thermal stability with respect to FMT polymorphs that enable its use in commercial formulations. Single crystals of the salt were obtained by the solvent evaporation method (FMT-MLT) and microcrystalline powder was synthesized by the comilling procedure (FMT-MLT_{CM}). Both synthesis methods were performed from a commercial mixture of A- and B-FMT leading to a unique compound, without requiring the previous polymorphic separation that might produce an increase in the production costs. Single-crystal X-ray diffraction determines that FMT moiety in FMT-MLT adopts an extended conformation that is stabilized by intramolecular H-bonds. The three-dimensional packing shows a complex pattern of H-bonds. These interactions generate infinite tapes along the *b* axis and columns along the *c* one. Adjacent tapes show nonconventional π - π stacking interactions between the thiazole and the quasiaromatic rings. The vibrational behavior is consistent with the structural findings. Thermal studies indicate that the salt melts at a higher temperature than the A-FMT and the pharmacologically preferred polymorph B. Finally, solubility experiments in water and SGF demonstrated that FMT-MLT exhibits a better performance than FMT polymorphs A and B.

ACKNOWLEDGMENTS

The authors thank the Consejo Nacional de Investigaciones Científicas y Técnicas (CONICET: PIP 112-201101-00912), Universidad Nacional de San Luis (SECyT-UNSL Project 2-1612). This work was supported by CNPq (Conselho Nacional de Desenvolvimento Científico e Tecnológico, Brazil). We are also grateful to Laboratório multiusuário for X-ray diffraction data collection in ApexII Bruker: Facility para Estudos Avançados de Materiais/FAMa (projeto FAPESP No. 2009/54035-4). M.G.R. acknowledges a PhD CONICET fellowship. G.E.N. is a member of CIC-CONICET.

REFERENCES

1. Lu J, Rohani S. 2010. Synthesis and preliminary characterization of sulfamethazine-theopyline co-crystal. *J Pharm Sci* 99:4042–4047.

2. Almarsson Ö, Zaworotko MJ. 2004. Crystal engineering of the composition of pharmaceutical phases. Do pharmaceutical co-crystal represent a new path to improved medicines? *Chem Comm* 17:1889–1896.
3. Nauha E, Kolehmainen E, Nissinen M. 2011. Packing incentives and a reliable N-H...N-pyridine synthon in co-crystallization of bipyridines with two agrochemical actives. *Cryst Eng Comm* 13:6531–6537.
4. Childs SL, Stahly GP, Park A. 2007. The salt-cocystal continuum: The influence of crystal structure on ionization state. *Mol Pharm* 4:323–338.
5. Bolla G, Nangia A. 2012. Clofazimine mesylate: a high solubility stable salt. *Cryst Growth Des* 12(12):6250–6259.
6. Karpinski PH. 2006. Polymorphism of active pharmaceutical ingredients. *Chem Eng Technol* 29:233–237.
7. Pangarkar PA, Tayade AM, Uttarwar SG, Wanare RS. 2013. Drug polymorphism: An overview. *Int J Pharm Tech* 5:2374–2402.
8. Morissette SL, Soukasene S, Levinson D, Cima MJ, Almarsson O. 2003. Elucidation of crystal form diversity of the HIV protease inhibitor ritonavir by high-throughput crystallization. *Proc Natl Acad Sci USA* 100:2180–2184.
9. Chan H, Doelker E. 1985. Polymorphic transformation of some drugs under compression. *Drug Dev Ind Pharm* 11:315–322.
10. Pirttimäki J, Laine E, Ketolainen J, Paronen P. 1993. Effect of grinding and compression on crystal structure of anhydrous caffeine. *Int J Pharm* 95:93–99.
11. Heinz A, Strachan CJ, Gordon KC, Rades T. 2009. Analysis of solid state transformations of pharmaceutical compounds using vibrational spectroscopy. *J Pharm Biopharm* 61:971–988.
12. Food and Drug Administration, Center for Drug Evaluation and Research. 2007. Guidance for industry, ANDA: Pharmaceutical solid Polymorphism: Chemistry, manufacturing, and controls information.
13. Liebenberg W, Dekker TG, Lötter AP, De Villiers MM. 1998. Identification of the mebendazole polymorphic form present in raw materials and tablets available in South Africa. *Drug Dev Ind Pharm* 24:485–488.
14. Ayala AP, Siesler HW, Cuffini SL. 2008. Polymorphism incidence in commercial tablets of mebendazole: A vibrational spectroscopy investigation. *J Raman Spectrosc* 9:1150–1157.
15. Paula K, Camí GE, Brusau EV, Narda GE, Ellena J. 2013. Mebendazole mesylate monohydrate: A new route to improve the solubility of mebendazole polymorphs. *J Pharm Sci* 102:3528–3538.
16. Brusau EV, Camí GE, Narda GE, Cuffini S, Ayala AP, Ellena J. 2008. Synthesis and characterization of a new mebendazole salt: Mebendazole hydrochloride. *J Pharm Sci* 97:542–552.
17. Cruz-Cabeza AJ, Bernstein J. 2013. Conformational polymorphism. *Chem Rev* 114:2170–2191.
18. Overgaard J, Hibbs DE. 2004. The experimental electron density in polymorphs A and B of the anti-ulcer drug famotidine. *Acta Crystallogr Sect A* 60:480–487.
19. Snider DA, Addicks W, Owens W. 2004. Polymorphism in generic drugs product development. *Adv Drug Deliv Rev* 56:335–347.
20. Cheng WT, Lin SY. 2008. Famotidine polymorphic transformation in the grinding process significantly depends on environmental humidity or water content. *Int J Pharm* 357:164–168.
21. Amidon GL, Lennernäs H, Shah VP, Crison JR. 1995. A theoretical basis for a biopharmaceutic drug classification: The correlation of in vitro drug product dissolution and in vivo bioavailability. *Pharm Res* 12:413–420.
22. Ibrahim MA, El-Badry M. 2013. Formulation of immediate release pellets containing famotidine solid dispersions. *Saudi Pharm J* 22(2):149–156.
23. Brettmann BK, Cheng K, Myerson AS, Trout B. 2013. Electrospun formulations containing crystalline active pharmaceutical ingredients. *Pharm Res* 30:238–246.
24. Maniruzzaman M, Rana MM, Boateng JS, Mitchell JC, Douroumis D. 2013. Dissolution enhancement of poorly water-soluble APIs processed by hot-melt extrusion using hydrophilic polymers. *Drug Dev Ind Pharm* 39:218–227.
25. Mady FM, Abou-Taleb AE, Khaled KA, Yamasaki K, Iohara D, Ishiguro T, Hirayama F, Uekama K, Otagiri M. 2010. Enhancement of the aqueous solubility and masking the bitter taste of famotidine using drug/SBE- β -CyD/Povidone K30 complexation approach. *J Pharm Sci* 99:4285–4294.
26. Mady FM, Abou-Taleb AE, Khaled KA, Yamasaki K, Iohara D, Tagauchi K, Anraku M, Hirayama F, Uekama K, Otagiri M. 2010. Evaluation of carboximethyl- β -cyclodextrin with acid function: Improvement of chemical stability, oral bioavailability and bitter taste of famotidine. *Int J Pharm* 397:1–8.
27. Patel AR, Vavia PR. 2008. Preparation and evaluation of taste masked famotidine formulation using drug/ β -cyclodextrin/polymer ternary complexation approach. *AAPS Pharm Sci Tech* 9:544–550.
28. Patel DJ, Patel JK, Pandya VM. 2010. Improvement in the dissolution of poorly water soluble drug using media milling technique. *Thai J Pharm Sci* 34:155–164.
29. Brittain HG. 2007. Strategy for the prediction and selection of drug substance salt forms. *Pharm Tech* 31(10):78–88.
30. Brittain HG. 2009. Developing an appropriate salt form for an active pharmaceutical ingredient. *Amer Pharm Rev* 12(7):62–65.
31. US Food and Drug administration approved GRAS list. <http://www.fda.gov/food/ingredientspackaginglabeling/gras>.
32. Hassan MA, Salem MS, Sueliman MS, Najib NM. 1997. Characterization of famotidine polymorphic forms. *Int J Pharm* 149:227–232.
33. Bruker APEX2 software v2011.8-0. Madison, Wisconsin. Bruker-AXS Inc. 2011.
34. SAINT integration software, v7.68A. Madison, Wisconsin. Bruker-AXS Inc. 2011.
35. Sheldrick GM. 1996. SADABS: Program for empirical absorption correction of area detector data. Göttingen, Germany: University of Göttingen.
36. Blessing R. 1995. An empirical correction for absorption anisotropy. *Acta Crystallogr A* 51(1):33–38.
37. Sheldrick GM. 1997. SHELXL-97: Program for Crystal Structures Analysis. University of Göttingen, Germany.
38. Sheldrick GM. 2008. A short history of SHELX. *Acta Crystallogr A* 64:112–122.
39. Bruno IJ, Cole JC, Kessler M, Luo J, Motherwell WDS, Purkis LH, Smith BR, Taylor R, Cooper RI, Harris SE, Orpen AG. 2004. Retrieval of crystallographically-derived molecular geometry information. *J Chem Inf Comput Sci* 4:2133–2144.
40. Farrugia L. 1997. ORTEP-3 for Windows—A version of ORTEP-III with a graphical user interface (GUI). *J Appl Cryst* 30(5 Part 1):565.
41. Macrae CF, Edgington PR, McCabe P, Pidcock E, Shields GP, Taylor R, Towler M, van de Streek J. 2006. Mercury: Visualization and analysis of crystal structures. *J Appl Cryst* 39:453–457.
42. Farrugia L. 1999. WinGX suite for small-molecule single-crystal crystallography. *J Appl Cryst* 32:837–838.
43. Raczynska ED, Cyranski MK, Gutowski M, Rak J, Gal JF, Maria C, Darowska M, Duczmal K. 2003. Consequences of proton transfer in guanidine. *J Phys Org Chem* 16:91–106.
44. Giacovazzo C. 2006. Fundamentals of crystallography. 3rd ed. New York: Oxford University Press.
45. Gilli G, Bellucci F, Ferretti V, Bertolasi V. 1989. Evidence for resonance-assisted hydrogen bonding from crystal-structure correlations on the enol form of the beta-diketone fragment. *J Am Chem Soc* 111:1023–1028.
46. Karabiyik H, Karabiyik H, Iskeleli ON. 2012. Hydrogen-bridged chelate ring-assisted π -stacking interactions. *Acta Crystallogr B* 68:71–79.
47. Lin SH, Cheng WT, Wang SL. 2006. Thermodynamic and kinetic characterization of polymorphic transformation of famotidine during grinding. *Int J Pharm* 318:86–91.

48. Cheng WT, Lin SY. 2008. Famotidine polymorphs transformation in the grinding process significantly depends on environmental humidity or water content. *Int J Pharm* 357:164–168.

49. Pretsch E, Clerc T, Seibl J, Simon W. 1998. *Tablas para la elucidación estructural de compuestos orgánicos por métodos espectroscópicos*. Singer Verlag-Ibérica. Barcelona, España.

50. Trask AV, Jones W. 2005. *Organic solid state reactions*; Toda F, Ed. Berlin, Germany: Springer Press.

51. Mallick S, Pattnaik S, Swain K, Saha A, Ghoshal G, Mondal A. 2008. Formation of physically stable amorphous phase of ibuprofen by solid state milling with kaolin. *Eur J Pharm Biopharm* 68:346–351.

52. Lu J, Wang XJ, Yang X, Ching CB. 2007. Polymorphism and crystallization of famotidine. *Cryst Growth Des* 7:1590–1598.

53. Wu Y, Fassih R. 2005. Stability of metronidazole, tetracycline HCl, and famotidine alone and in combination. *Int J Pharm* 290:1–13.